POLITECNICO DI TORINO
Repository ISTITUZIONALE

The Role of Cation Acidity on the Competition between Hydrogen Evolution and CO2 Reduction on Gold Electrodes

(Article begins on next page)

18 November 2024

The Role of Cation Acidity on the Competition between Hydrogen Evolution and CO₂ Reduction on Gold Electrodes

Mariana C. O. Monteiro, Federico Dattila, Núria López, and Marc T. M. Koper*

ACCESS | Metrics & More | Article Recommendations | Supporting Information

ABSTRACT: CO₂ electroreduction (CO₂RR) is a sustainable alternative for producing fuels and chemicals. Metal cations in the electrolyte have a strong impact on the reaction, but mainly alkali species have been studied in detail. In this work, we elucidate how multivalent cations (Li^+, Cs^+, Be^{2+}, Mg^{2+}, Ca^{2+}, Ba^{2+}, Al^{3+}, Nd^{3+}, and Ce^{3+}) affect CO₂RR and the competing hydrogen evolution by studying these reactions on polycrystalline gold at pH = 3. We observe that cations have no effect on proton reduction at low overpotentials, but at alkaline surface pH acidic cations undergo hydrolysis, generating a second proton reduction regime. The activity and onset for the water reduction reaction correlate with cation acidity, with weakly hydrated trivalent species leading to the highest activity. Acidic cations only favor CO₂RR at low over-

potentials and in acidic media. At high overpotentials, the activity for CO increases in the order $Ca^{2+} < Li^+ < Ba^{2+} < Cs^+$. To favor this reaction there must be an interplay between cation stabilization of the $*CO_2^-$ intermediate, cation accumulation at the outer Helmholtz plane (OHP), and activity for water reduction. *Ab initio* molecular dynamics simulations with explicit electric field show that nonacidic cations show lower repulsion at the interface, accumulating more at the OHP, thus triggering local promoting effects. Water dissociation kinetics is increasingly promoted by strongly acidic cations (Nd^{3+}, Al^{3+}), in agreement with experimental evidence. Cs^+, Ba^{2+}, and Nd^{3+} coordinate to adsorbed CO₂ steadily; thus they enable $*CO_2^-$ stabilization and barrierless protonation to COOH and further reduction products.
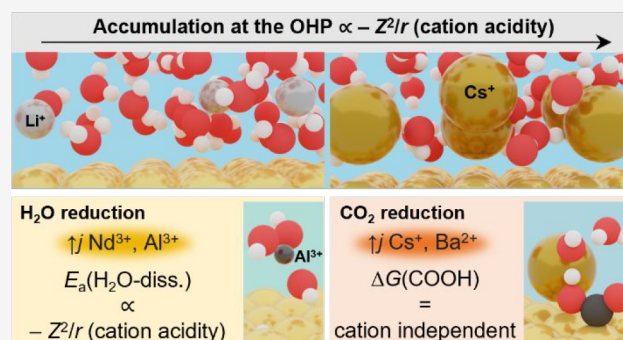
INTRODUCTION

The electrochemical reduction of carbon dioxide (CO₂RR) offers a sustainable pathway to produce fuels or base chemicals without relying on finite and nonrenewable resources such as oil and gas.[1−3] During CO₂RR in aqueous electrolyte, the hydrogen evolution reaction (HER) occurs concomitantly, which may significantly lower the faradaic efficiency of CO₂RR.[4−6] Depending on the reaction conditions, specifically the electrolyte pH, the production of hydrogen can happen through either the direct reduction of protons ($2H^+ + e^- \rightarrow H_2$) or the reduction of the solvent itself ($2H_2O + 2e^- \rightarrow H_2 + 2OH^-$). Different strategies have been adopted to favor CO₂RR over HER, such as enhancing mass transport,[6] using porous catalysts,[7,8] or modifying the catalyst surface.[9] An alternative approach is to change the electrolyte composition, since the cation identity, for instance, is known to highly influence both the CO₂RR[10−12] reaction and HER[13,14] rates. Up to now, mainly alkali cations have been employed for CO₂RR, but recent theoretical work suggests that multivalent cations may lead to an even larger enhancement of the reaction activity.[11] Still, in order to use that in favor of the CO₂RR in aqueous media, one also has to understand how cation properties affect the competing HER.

Since the work of Hori and co-workers, it is known that the species in the electrolyte can influence the product selectivity and faradaic efficiency of the CO₂RR.[15−17] Despite the strong effect that cations have on CO₂RR, mainly alkali metals in neutral or alkaline media have been investigated using copper,[11] silver,[18] or gold[19,20] electrodes. It has been established that the CO₂RR activity increases in the order $Li^+ < Na^+ < K^+ < Cs^+$. Three main theories have been suggested to explain this trend, namely, local buffering at the interface,[21] changes in the (local) electric field,[11,22,23] and electrostatic interactions with reaction intermediates.[22,24] In a recent work, we elucidated that the key specific role of cations on CO₂RR to CO is to stabilize the negatively charged reaction intermediate, $*CO_2^-$.[25] We observe that without a metal cation in the electrolyte, CO is not produced on gold, silver, and copper electrodes. Through *ab initio* molecular dynamics

simulations, we showed that besides the medium-range electric field/adsorbate dipole interaction at the interface, there is an explicit short-range local electrostatic interaction between the partially desolvated metal cations and CO_2. Additionally, we observe that the activity trend reported for alkali cations originates from both different cation concentrations at the outer Helmholtz plane (OHP) and their different intrinsic ability to coordinate to adsorbed CO_2^-. In the alkali cations group, these vary from low concentrations and almost no bond for Li^+ to higher concentrations in the OHP and almost double coordination between the cation and CO_2 oxygens for Cs^+.

Considering the previously discussed key role of cations on CO_2RR, it would be attractive to find cationic species that can have an even larger stabilizing effect on CO_2 than Cs^+ and perhaps accumulate at the OHP at higher concentrations, such as large multivalent cations[26] or surfactants.[27] One of the few experimental works on the effect of multivalent cations on CO_2RR was carried out by Schizodimou and Kyriacou,[26] who reported that multivalent cations increase the rate of CO_2RR on Cu(88)−Sn(6)−Pb(6) electrodes in highly acidic media (1.5 M HCl) and low overpotentials (−0.65 V vs Ag/AgCl). The authors observed that at more negative overpotentials the effect of the cations was less pronounced, and this was attributed to a change in the reaction rate-determining step. Although the electrolysis was performed for 2 h in each electrolyte, no comment was made in terms of salt deposition and/or electrode stability, which are factors that could strongly perturb the cation trends observed. For example, in our recent work on polycrystalline gold electrodes, after one HER cyclic voltammogram from 0 to −1.2 V vs RHE at 50 mVs^{-1} in $Al_2(SO_4)_3$ (argon saturated, pH 3) we observe deposition of a porous aluminum hydroxide layer on the whole surface.[28] Density functional theory (DFT) calculations presented in the work of Ringe et al.[11] also suggest that multivalent cations can have a beneficial effect on the activity of CO_2RR. They predicted the effect of cations on the activity toward CO on Ag(111) electrodes at −1 V vs RHE (in a nominal 0.1 M electrolyte) and theoretically predict that species such as Be^{2+}, Al^{3+}, Ba^{2+}, and La^{3+} should exhibit up to 2 orders of magnitude higher activity for CO than Cs^+, since their larger charge would enhance the interfacial electric field. In contrast, Bhargava et al.[29] recently reported that multivalent cations hinder the electrochemical reduction of CO_2 to CO on silver gas diffusion electrodes, due to the formation of deposits that block Ag active sites. Despite these apparently contradictory predictions and results, in the work of Schizodimou and Kyriacou,[26] Ringe et al.,[11] and Bhargava et al.,[29] the effect of multivalent cations on the competing hydrogen evolution reaction was not discussed. How cations influence the activity of the competing HER on copper surfaces has not been studied in detail. However, on gold and silver electrodes, for instance, the activity for water reduction in alkaline media increases in the order $Li^+ < Na^+ < K^+ < Cs^+$, in solutions of neutral to alkaline pH and relatively low cation concentration.[14,30] In acidic media, we previously observed that alkali cations have no significant effect on proton reduction,[25] while Al^{3+} seems to give rise to an additional proton diffusion-limited regime at more cathodic potentials.[28] However, to fully understand the interplay between CO_2RR and HER activity and how cation properties (hydration radius, charge, etc.) play a role, a more systematic study is required.

Therefore, in this work we have studied HER and CO_2RR on polycrystalline gold electrodes with the aim to determine how different mono- and multivalent metal cations (Li^+, Cs^+, Be^{2+}, Mg^{2+}, Ca^{2+}, Ba^{2+}, Al^{3+}, Nd^{3+}, and Ce^{3+}) affect the individual reaction rates. We find that acidic cations with a moderate hydration radius (Nd^{3+}, Ce^{3+}) promote CO_2RR in acidic media/low overpotentials, while the nonacidic, weakly hydrated Cs^+ is the cation that promotes CO_2RR the most in alkaline media/high overpotentials. These differences come from the extreme promotional effects that acidic cations have on water reduction at high overpotentials. We further probed the interaction of the different cations with water and CO_2 using *ab initio* molecular dynamics simulations with both explicit electric field and explicit solvation. The simulations highlight three key parameters for CO_2RR performance ruled by cation acidity: cation accumulation at the OHP, water dissociation kinetics, and cation−CO_2 coordination. Overall, in this work, we elucidate through a combination of experiments and simulations which cation properties are important to consider when designing an optimal electrolyte for the CO_2RR and/or HER systems.

■ EXPERIMENTAL SECTION

Electrode Preparation. Gold disc electrodes (8 mm diameter) were cut from a polycrystalline gold foil (0.5 mm thick, MaTecK, 99.995%) and prepared by polishing and flame annealing according to the procedure we have previously described.[28] The gold electrode cleanliness was assured by scanning electron microscopy (SEM) performed using an Apreo SEM (ThermoFisher Scientific). Micrographs were obtained using an acceleration voltage of 10 kV and an electron beam current of 0.4 nA. Additionally, elemental analysis of the surface composition was performed using energy dispersive X-ray spectrometry (EDX) (Oxford Instruments X-Max^N 150 silicon drift detector). The EDX data were processed using the Pathfinder X-ray Microanalysis software v1.3. The SEM micrographs and EDX spectra are shown in Figure S1 in the Supporting Information (SI). Establishing surface cleanliness is crucial when studying cation effects on CO_2RR and HER, as we have previously shown that, for instance, polishing alumina particles can contaminate the gold surface and promote water reduction by the release of Al^{3+} ions in an acidic electrolyte.[28]

Materials. Appropriate amounts of the following salts were employed to prepare the electrolytes used in this work: Li_2SO_4 (Alfa Aesar, anhydrous, 99.99%, metal basis), Na_2SO_4 (Alfa Aesar, anhydrous, 99.99%, metal basis), K_2SO_4 (Sigma-Aldrich, anhydrous, 99.99%, metal basis), Cs_2SO_4 (Alfa Aesar, Puratronic, 99.997%, metal basis), $BeSO_4$ (Alfa Aesar, tetrahydrated, 99.99%, metal basis), $MgSO_4$ (Sigma-Aldrich, ≥99.99%, trace metal basis), $Al_2(SO_4)_3$ (Sigma-Aldrich, 99.99%, trace metal basis), $Nd_2(SO_4)_3$ (Sigma-Aldrich, 99.99%, trace metal basis), $Ce_2(SO_4)_3$ (Sigma-Aldrich, ≥99.99%, trace metal basis), $LiClO_4$ (Sigma-Aldrich, 99.99%, trace metal basis), $CsClO_4$ (Sigma-Aldrich, 99.99%, trace metal basis), $Mg(ClO_4)_2$ (American Elements, 99.99%), $Ca(ClO_4)_2$ (American Elements, tetrahydrated, 99.99%), $Ba(ClO_4)_2$ (Sigma-Aldrich, 99.999%), Li_2CO_3 (Merck, 99.99%, trace metal basis), $NaHCO_3$ (Sigma-Aldrich, ≥99.7%, ACS reagent), $KHCO_3$ (Sigma-Aldrich, ≥99.95%, trace metal basis), Cs_2CO_3 (Merck, 99.9%, trace metal basis), and H_2SO_4 (Merck, Suprapur, 96%). The carbonate and bicarbonate electrolytes were purified by long-term electrolysis prior to the experiments. Two large surface area gold electrodes were used, and a potential of −2 V was applied for 12 h, similarly to the procedure reported elsewhere.[31] The sulfates and perchlorates were used as received, as these are high-purity salts, ≥99.99%. The pH of the prepared electrolyte was certified using a glass-electrode pH meter (Lab 855, SI Analytics) calibrated with standard buffer solutions (Radiometer Analytical). The experiments were performed in a one-compartment, three-electrode cell with the gold working electrode in hanging meniscus configuration. The glassware used in this work was stored in potassium permanganate solution (1 g L^{-1} $KMnO_4$
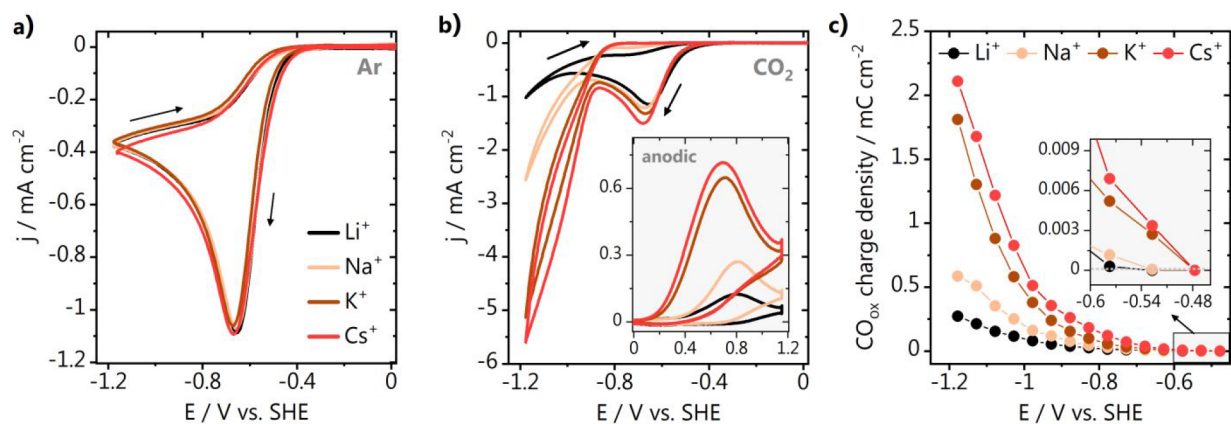
Figure 1. Cyclic voltammetry of (a) proton reduction and (b) CO_2 reduction in acidic media (0.1 M M_2SO_4, pH = 3). (c) Amount of CO produced as a function of potential, obtained by consecutive cathodic/anodic voltammetry.

dissolved in 0.5 M H_2SO_4) overnight and cleaned by immersion in dilute piranha (3:1 v/v mix of H_2SO_4 (96%)/H_2O_2 (30%), diluted with water). Subsequently, the glassware was boiled at least five times in ultrapure water (>18.2 MΩ cm, Millipore Milli-Q). A gold wire (0.8 mm thick, Mateck, 99.9%) was used as counter electrode and a reversible hydrogen electrode (RHE) or a Hydroflex (Gaskatel) as reference, connected to the cell via a Luggin capillary.

Electrochemical Measurements. Experiments were carried out using a Bio-Logic potentiostat/galvanostat/EIS (SP-300). The gold electrode was characterized before each experiment by recording a cyclic voltammogram between 0 and 1.75 V vs RHE in 0.1 M H_2SO_4 at 50 mV s^{-1}. The gold electrochemical surface area (ECSA) was determined by calculating the charge corresponding to the gold oxide reduction. This value was converted to ECSA using the charge density associated with the reduction of a monolayer of gold oxide (386 μC cm^{-2}, assuming a roughness factor of 1).[32] Hydrogen evolution or CO_2 reduction was conducted after purging the electrolyte with either argon or CO_2 for at least 20 min. During the experiments, the respective gas flow was kept above the electrolyte, to avoid oxygen diffusion into the solution. Before each measurement, the solution resistance was determined by electrochemical impedance spectroscopy (EIS) and the electrode potential was compensated for 85% of the ohmic drop. The potential opening CO_2 reduction experiments were performed by cycling the gold electrode from 0.1 V vs RHE to different negative potentials and in the reverse scan up to 1.3 V vs RHE. In between two different potential steps the electrode potential was held at 0.1 V vs RHE for 4 min to recover from the concentration (pH) gradients developed in the diffusion layer during the cathodic scan.

Density Functional Theory and *ab Initio* Molecular Dynamics Modeling. DFT simulations were performed using the Vienna Ab Initio Simulation Package (VASP),[33,34] with the PBE density functional.[35] To properly account for dispersion, we applied the DFT-D2 method,[36,37] with the C_6 coefficients reparametrized from one of our groups.[38] Inner electrons were represented by PAW pseudopotentials,[39,40] and the monoelectronic states for valence electrons were expanded as plane waves with a kinetic energy cutoff of 450 eV. *Ab initio* molecular dynamics (AIMD) simulation was applied on the Au/water/cation system (see Computational Models) for 4 ps (1 fs time step) in a canonical NVT ensemble at 300 K regulated by a Nosé–Hoover thermostat.[25,41–43] To account for the self-interaction error due to the localized f electrons of Nd^{3+}, we applied a Hubbard correction U_{eff} = 6.76 eV − 0.76 eV following Dudarev's approach,[44] taken from a study of electronic and magnetic properties of a Nd adatom.[45]

■ **RESULTS**

Effect of Alkali Cations on Proton, Water, and CO_2 Reduction. To better understand how different metal cations

(M^{n+}) affect the competition between the CO_2RR and HER, we studied these reactions through cyclic voltammetry using polycrystalline gold electrodes. First, we studied the effect of alkali cations on HER and CO_2RR in acidic electrolytes (pH 3, 0.1 M M_2SO_4), with M^{n+} = Li^+, Na^+, K^+, and Cs^+. Hydrogen evolution was carried out in argon-purged solutions as shown in Figure 1a, where a cathodic current due to proton reduction starts at about −0.35 V vs SHE, and a peak due to proton diffusion limitation is observed at −0.66 V vs SHE. At more negative potentials, the current decreases as the diffusion layer thickness increases. We find that the cation identity does not affect the proton reduction current, in both the kinetic and diffusion-limited regimes, in agreement with our previous work, where the reaction was carried out in more dilute electrolytes.[25] We also performed cyclic voltammetry (CV) in a CO_2 atmosphere (Figure 1b) in order to distinguish the HER current from the CO_2RR current. At potentials more negative than −0.6 V vs SHE, an increase in the total current is observed in the order Cs^+ > K^+ > Na^+ > Li^+. Moreover, CO_2 reduction happens in parallel to proton reduction already at low overpotentials, with Cs^+ leading to the highest activity. As the potential is scanned more negatively and the concentration of protons near the surface decreases, a kinetic reduction current appears, which is a contribution from both water and CO_2 reduction and follows the same cation trend. In a consecutively recorded positive-going scan (inset of Figure 1b) a faradaic current is observed due to the oxidation of the CO produced after polarizing the electrode negatively, which in this work we employ as a semiquantitative analysis of the amount of CO produced. Blank CVs of the gold electrode before the measurements are shown in Figure S2 in the SI.

This consecutive cathodic/anodic voltammetry is used here as a semiquantitative tool to selectively probe the amount of CO produced during CO_2RR as a function of potential, *in situ*, and with high sensitivity. Basically, after polarizing the gold electrode at different negative potentials, a positive-going scan is recorded until 1.3 V so the CO produced in the cathodic scan is directly oxidized at the electrode surface. After each measurement, the electrode potential is held for 4 min in the double-layer region to restore the diffusion layer and bring the pH near the surface back to the bulk pH at the beginning of each cycle. The voltammetry of these potential opening experiments can be seen in Figure S3 in the SI, for measurements performed in CO_2-saturated 0.1 M M_2SO_4, pH = 3. The amount of CO produced at every potential was
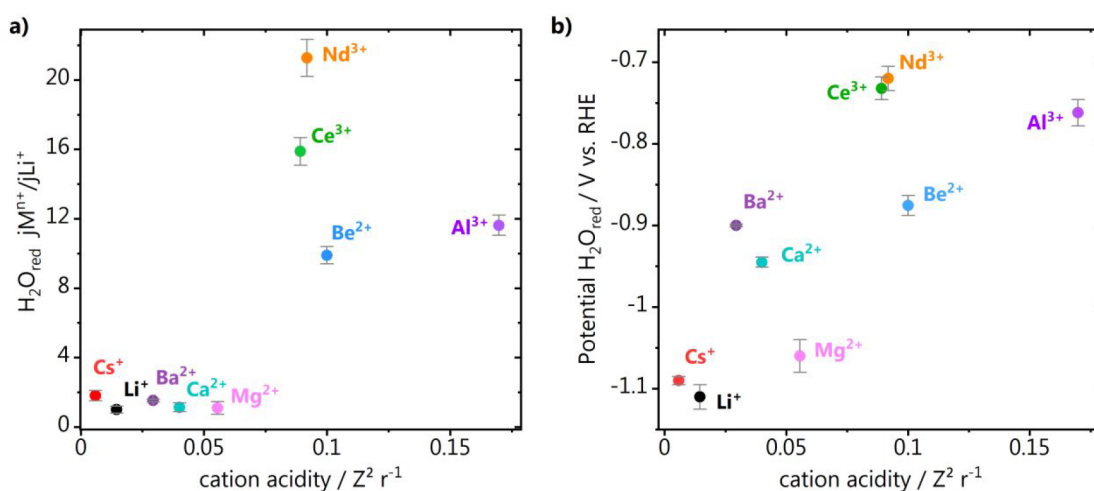
Figure 2. Effect of multivalent cations on HER. (a) Normalized activity for water reduction extracted from the hydrogen evolution voltammetry performed at pH 3 in 0.1 M Li_2SO_4 + 1 mM M^{n+} electrolytes with M^{n+} = Li^+, Cs^+, Be^{2+}, Mg^{2+}, Al^{3+}, Nd^{3+}, Ce^{3+} and 0.2 M $LiClO_4$ + 2 mM M^{n+} with M^{n+} = Ca^{2+}, Ba^{2+}. The normalization was done by dividing the water reduction current density (at −1.1 V vs RHE) in 0.1 M Li_2SO_4 + 1 mM M^{n+} by the current density obtained in pure 0.1 M Li_2SO_4. The same was done for the measurements in perchlorate. (b) Potentials at which the activity for water reduction strongly increases, obtained by taking the derivative of the CVs from Figure S7a and the CVs for Ba^{2+} and Ca^{2+} from Figure S7b. All electrolytes were saturated with argon prior to the measurements. Error bars (s.d.) were calculated based on three individual measurements.

obtained by integrating the CO oxidation CVs and subtracting the double-layer charge. We see in Figure 1c that the activity for CO production increases in the order Li^+ < Na^+ < K^+ < Cs^+ in the whole potential range. This trend is in agreement with literature and our previous work,[25] showing that the consecutive cathodic/anodic voltammetry method presented here is a reliable tool to probe activity for CO with high sensitivity. However, here we see that in the Cs^+ and K^+ electrolyte more CO is produced already at lower potentials than in Na^+ and Li^+ (see the figure inset). This is due to the higher concentration of these weakly hydrated cations near the surface at these potentials and the higher capability of Cs^+ and K^+ to coordinate with the adsorbed CO_2^- reaction intermediate.[25] Similar experiments as shown in Figure 1a and b were carried out in alkaline media (0.1 M $MHCO_3$) and are shown in Figure S5a and b. We find that the activity for water reduction is higher in solutions containing weakly hydrated cations and increases in the order Li^+ < Na^+ < K^+ < Cs^+, in agreement with what was previously reported by Xue et al. for HER on Au(111) in MOH electrolytes.[30] The activity for CO_2 reduction in bicarbonate electrolyte follows the same trend with alkali cation identity as water reduction, which means that differently from acidic media, here the alkali cations cannot be used to exclusively favor the CO_2 reduction reaction over HER.

Here, we observed that alkali cations do not have any effect on proton reduction, while the activity for CO_2RR to CO and water reduction increases in the order Li^+ < Na^+ < K^+ < Cs^+. We see that the consecutive cathodic/anodic voltammetry method that we present here can be used to reliably probe activity for CO even at low overpotentials, which will be valuable in the next section, where we look at multivalent cation species. The advantage is that we are not strongly hindered by detection limits, which is the case for other commonly used product detection techniques, such as gas chromatography. In the next sections we probe the effect of mono- and multivalent cations, first on hydrogen evolution

(proton and water reduction) and then on CO_2 reduction, both experimentally and through simulations.

Effect of Multivalent Cations on Proton and Water Reduction. To further elucidate which cation properties determine the activity for HER, we performed cyclic voltammetry on polycrystalline gold at pH 3 in electrolytes containing the following mono- and multivalent metal cations: Li^+, Cs^+, Be^{2+}, Mg^{2+}, Ca^{2+}, Ba^{2+}, Al^{3+}, Nd^{3+}, and Ce^{3+}. In acidic media (pH = 3) all cations investigated are fully soluble, although we have previously reported that acidic cations such as Al^{3+} may reversibly deposit on gold as layered hydroxides during HER, upon an increase in the local alkalinity caused by the surface reaction.[28] To minimize this possible deposition, either 0.1 M Li_2SO_4 or 0.2 M $LiClO_4$ was used here as background electrolyte and only 1% of a given mono- or multivalent cation M^{n+} was added to the solution. A 1 mM concentration of M^{n+} was added to 0.1 M Li_2SO_4 background, and 2 mM M^{n+} was added to the 0.2 M $LiClO_4$, keeping the Li^+ concentration and the M^{n+}/Li^+ ratio constant. Solutions of these two anions were used because not all sulfate/perchlorate salts containing the multivalent cations are available or soluble. Additionally, using a Li^+-containing electrolyte as background allows us to normalize the data to the results in pure Li^+ and to consequently make a qualitative comparison between sulfates and perchlorates. The following cations were studied in the Li_2SO_4 electrolyte: Cs^+, Be^{2+}, Mg^{2+}, Al^{3+}, Nd^{3+}, and Ce^{3+}, while Ca^{2+} and Ba^{2+} were added to $LiClO_4$. We performed the measurements in argon-saturated electrolyte and evaluated how the different cations influence the activity for proton (at low overpotential) and water reduction (at high overpotential). The HER cyclic voltammetry is available in the SI together with the blank voltammograms of the gold electrode, recorded before each measurement (Figure S8 and Figure S9). In the cyclic voltammetry (Figure S9), we see that similarly to the alkali cations, the multivalent species do not affect the current of the first regime of proton reduction (cathodic peak at low overpotential). Although the metal cation in solution does not seem to have an effect, comparing the proton reduction current
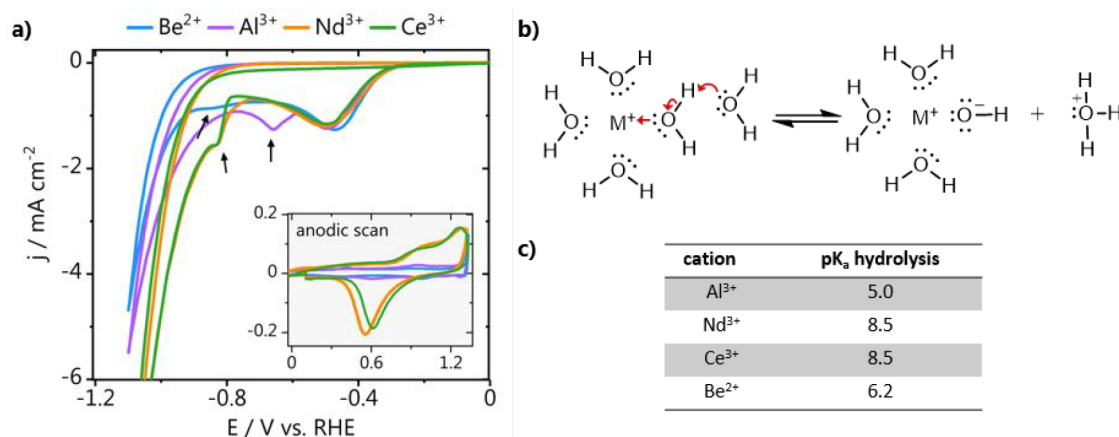
Figure 3. (a) Hydrogen evolution cyclic voltammetry performed at pH 3 in 0.1 M Li_2SO_4 + 1 mM M^{n+} electrolytes with M^{n+} = Be^{2+}, Al^{3+}, Nd^{3+}, and Ce^{3+}. An anodic scan recorded directly after HER is shown in the graph inset. (b) Schematic representation of the mechanism of cation hydrolysis and (c) pK_a of hydrolysis of the different species, taken from ref 36.

obtained in the sulfate and perchlorate electrolytes (both pH 3), a more negative proton reduction current is found in sulfate. This is due to the stronger buffer capacity of the sulfate electrolyte, which leads to fewer changes in local pH and consequently a higher proton concentration at the electrode/electrolyte interface.

While the effect of multivalent cations on proton reduction at low overpotential is subtle, we see in Figure S9 that they have a strong effect on water reduction, with much more pronounced differences than previously observed for the alkali cations (Figure S5). Figure 2a shows a comparison of the activity for water reduction in the presence of the different cations, normalized to the activity obtained in the pure lithium (sulfate or perchlorate) electrolytes. The activity is compared in terms of the water reduction current density obtained at -1.1 V vs RHE, with the exception of Li^+, Mg^+, and Cs^+, which only show high activity for water reduction at more negative potentials. For these, the current density at -1.2 V vs RHE was used. We see in Figure 2a the relative activity plotted as a function of the cation acidity, which is defined as the ratio of the cation charge and its ionic radius (derived from the Born equation).[46] Trivalent cations and Be^{2+} lead to the highest activity for water reduction, whereas the divalent and monovalent species give a much lower (and similar) activity. In fact, within a valence group, we observe that the highest activity is always found for the weaklier hydrated cations: Nd^{3+} and Ce^{3+}, Ba^{2+} and Cs^+. This is likely due to their higher concentration at the OHP at a given potential. In Figure 2b we see the effect of the different cations on the potential at which there is a strong increase in the activity for water reduction. This was determined by taking the derivative of the cyclic voltammograms from Figure S7 and extracting the potential where there is a change in slope. This represents the potentials at which the water reduction current significantly increases, which are shown in Figure 2b for the different cations. We observe that both the activity and water reduction "onset" potential show a strong correlation with the cation acidity. Even though the cations with a smaller ionic radius are more acidic, leading to weaker hydrogen bonds in the water molecules in their hydration shell, their high hydration/solvation energy hinders their accumulation near the surface. Therefore, the highest activity and earliest onset for water reduction are found for moderately acidic and relatively weakly

hydrated cations as Nd^{3+} and Ce^{3+}. We show in Figure S8 in the SI how the cation acidity is related to the Gibbs free energy of hydration or, in other words, to how strongly water molecules in the cation's hydration shell interact with the positive charge of the ion.[47] Considering that on gold the Volmer step (H_2O + e^- + * → *H + OH^-) is the rate-determining step for the water reduction reaction, acidic (trivalent) cations likely lead to a stronger stabilization of the transition state of the water dissociation step (eq 1).[14] This will be explored in more detail in the modeling section. It is also important to note that Be^{2+} is an outlier regarding the trends found in Figure 2: in solution, Be^{2+} behaves more like a trivalent species, due to the very high charge density of the beryllium atom, caused by its small size.[48]

$$H_2O + e^- + * + M^{n+}$$
$$\rightarrow *H{-}OH^{\delta-} \cdots M^{n+} + (1-\delta)e^-$$
$$\rightarrow *H + OH^- + M^{n+} \quad (1)$$
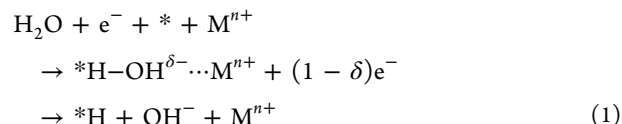
Cation Hydrolysis. As mentioned previously, we do not observe any significant effect of cations on the proton reduction current at low overpotentials, which we call here the first proton reduction regime. However, as shown in Figure 3a, in solutions containing very acidic cations, such as Be^{2+}, Al^{3+}, Nd^{3+}, and Ce^{3+}, a second proton reduction regime (indicated by the black arrows) is observed in the HER cyclic voltammetry at more negative potentials, due to hydrolysis of water molecules from the cation's hydration shell. This phenomenon had also been observed in our previous work, where micromoles of Al^{3+} were added to the electrolyte; however at the time this was still poorly understood.[28] As shown in the schematics of Figure 3b and the table in Figure 3c, when the pH in the surroundings of a cation reaches the pK_a of hydrolysis of that species, a hydronium ion is released into the electrolyte. The positive charge of the conjugated acid (metal cation) weakens the hydrogen bond of the water molecule by drawing the electron density of the oxygen toward the metal center, thus leading to the release of a proton in solution. The reaction can be expressed as shown in eq 2, considering water is the only complexing species, where n is the charge of the cation and N is the number of water molecules within its coordination shell.
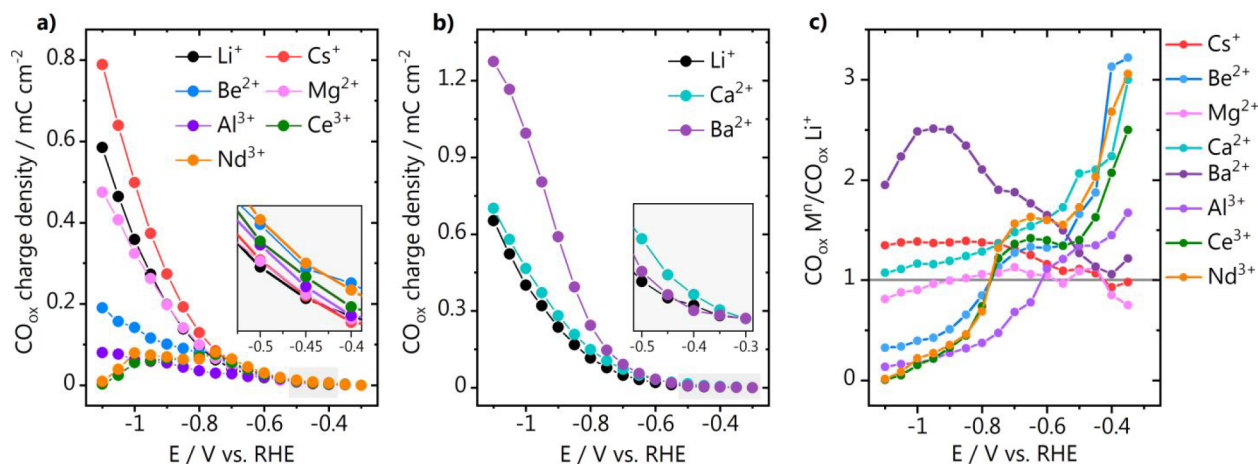
Figure 4. Amount of CO produced probed via consecutive cathodic/anodic voltammetry at pH 3 in (a) 0.1 M Li_2SO_4 + 1 mM M^{n+} electrolytes with M^{n+} = Li^+, Cs^+, Be^{2+}, Mg^{2+}, Al^{3+}, Nd^{3+}, Ce^{3+} and (b) 0.2 M $LiClO_4$ + 2 mM M^{n+} with M^{n+} = Ca^{2+}, Ba^{2+} and a (c) qualitative comparison between the relative activity for CO found in sulfate and perchlorate electrolyte at low and high overpotential, by normalizing the CO_{ox} charge density to the one found in the pure Li_2SO_4 and $LiClO_4$ background electrolytes.

$$M^{n+}(H_2O)_N \leftrightarrow MOH^{(n-1)+}(H_2O)_{N-1} + H^+ \qquad (2)$$
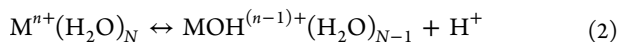
Once the local pH reaches the pK_a of hydrolysis of the different species, hydronium ions are produced locally and will be readily reduced at the surface, giving rise to the second proton reduction regime from Figure 3a. This happens at more acidic local pH (lower overpotentials) for Al^{3+} cations, in comparison to Be^{2+}, Nd^{3+}, and Ce^{3+}, as typically, the larger the charge and the smaller the radius, the lower the pH at which the metal cation will hydrolyze. Note that for Nd^{3+} and Ce^{3+}, which have the same pK_a, the second proton reduction regime indeed starts at nearly the same potential. Be^{2+} is again an exception, as it also forms complexes with the sulfate ions in the electrolyte, which delays the hydrolysis reaction.[49] Hao et al.[50] argue that Be^{2+} ions are protected from hydrolysis by the formation of $BeSO_4$ ion pairs and that most of the hydronium ions produced by hydrolysis are initially converted to bisulfate ions. For all cations shown in Figure 3a, as the local pH becomes more alkaline (due to the increase in water reduction current at more cathodic potentials), more water molecules undergo hydrolysis, forming polymeric species of various stoichiometries, depending on the cation charge, size, and coordination number.[51] Eventually, at sufficiently alkaline local pH, a solid hydroxide layer can form on the electrode surface, whose properties will depend on the temperature, anions, and ion concentration (eq 3), where n is the charge of the cation and N is the number of water molecules within its coordination shell.

$$M^{n+}(H_2O)_N \leftrightarrow MO_x(OH)_{n-2x}(s) + nH^+ + (N - n + x)$$
$$H_2O \qquad (3)$$
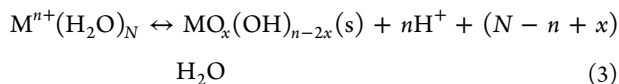
In our previous work, we observed that after recording five HER cyclic voltammograms of a polycrystalline gold electrode in a 0.1 M $Al_2(SO_4)_3$ electrolyte, ~200 nm thick porous hydroxide plates formed on the gold surface, intercalated by sulfate anions.[28] The formation of a thin hydroxide layer upon cycling is also observed here in the consecutive anodic cyclic voltammetry for the various cations (inset of Figure 3a), as evidenced by the shift and suppression in the gold oxide/reduction peaks. Five consecutive CVs can be seen in Figure S9 in the SI, where this effect is even more pronounced as the

proton reduction current decreases from cycle 1 to 5. However, due to the low amount (1%) of acidic cations in the lithium background electrolytes, after the 5 cycles are recorded and the electrode is held at 0.1 V for 4 min, the local pH goes back to the (acidic) bulk value and the hydroxide thin layer formed dissolves; indeed, no deposits are found in SEM/EDX analysis after these experiments (not shown).

We see that the first regime of proton reduction (at low overpotentials) is not influenced by the metal cations in the electrolyte. Still, acidic cations give rise to a second proton reduction regime, due to a local discharge of protons near the surface upon cation hydrolysis. The potential at which this is observed is a function of the pK_a of hydrolysis. For water reduction, we find that the activity increases going from mono- to di- to trivalent cations due to the effect that acidic cations have on the water dissociation step. Within a valence group, weakly hydrated cations lead to higher activity, as our previous study suggests that these species accumulate more at the OHP. Next, we investigate the consequences of these trends found for HER on the activity of CO_2 reduction, by carrying out the reaction in a CO_2 atmosphere in the same electrolytes from Figure 2.

Effect of Multivalent Cations on CO_2 Reduction. Figure 4 shows the activity for CO production as a function of potential in electrolytes containing different mono- and multivalent cations. CO_2RR was carried out in the same electrolytes as the measurements shown in Figure 2, and the CO produced as a function of potential was quantified using the consecutive cathodic/anodic voltammetry method we used for the alkali cations in Figure 1c. Figure 4a shows that in the sulfate electrolyte at high overpotentials the highest absolute activity for CO is found in the presence of Cs^+, followed by Li^+, Mg^+, Be^{2+}, Al^{3+}, Nd^{3+}, and Ce^{3+}. In the case of perchlorates, as shown in Figure 4b, more CO is formed at high overpotentials in the Ba^{2+} electrolyte, followed by Ca^{2+} and Li^+. This seems to contradict the predictions made in the work of Ringe et al.,[11] in which DFT calculations suggested that higher activity for CO_2RR to CO should be found in electrolytes containing trivalent cations, followed by divalent and monovalent (at −1 V vs RHE), since the electronic density at the surface is expected to increase accordingly. This is because in this study the authors disregard the effect of the

acidic multivalent cations on the competing water reduction reaction, which is the main branch of HER taking place at high overpotentials. In Figure 2a we see that the activity for water reduction in the presence of species as Be^{2+}, Al^{3+}, Nd^{3+}, and Ce^{3+} is more than 10 times higher than for the other cations, which explains why here, despite any promotional effect these cations may have on the CO_2RR, they actually favor even more the production of hydrogen.

Remarkably, looking at the absolute amounts of CO produced at low overpotentials (see the inset of Figure 4a and b), we see the opposite trend, where more CO is formed in the presence of more acidic cations. To make clearer the differences in activity for CO at low and high overpotentials, and to compare the results in sulfate with perchlorate, we normalized the CO_{ox} charge densities from Figure 4a and b to the CO_{ox} charge density obtained in the pure Li_2SO_4 or $LiClO_4$ background electrolytes, respectively. This results in the relative activities depicted in Figure 4c. Values above 1 represent cations that show higher activity for CO than Li^+ at a given potential, and values below 1 represent cations for which the CO_2RR is less active than in pure Li^+ electrolyte. Please note that these are only relative activities; that is, the higher ratio for Ba^{2+} does not mean CO_2RR is more active in a Ba^{2+} electrolyte than Cs^+, as these were measured with electrolytes of two different anions. We can, however, infer that in both Ba^{2+} and Cs^+ electrolytes the activity for CO is higher at large overpotentials. With that in mind, we see in the results from Figure 4c that at potentials more positive than −0.5 V vs RHE, the more acidic cations lead to the production of more CO. At these potentials, the main branch of HER competing with CO_2RR is proton reduction, which is a reaction that is not affected by the cation identity, meaning that here the cation can selectively enhance CO_2RR. As proton reduction is here still in the kinetic limited regime (see Figure 1a), the local pH is not expected to deviate too much from the bulk pH value, which means that in this regime cations will not rapidly undergo hydrolysis (which would favor proton reduction) but likely can still strongly interact with the reaction interface (enhancing CO_2 reduction). At potentials more negative than −0.6 V vs RHE, we see that the relative activity found in the presence of acidic cations drops, and higher relative activity for CO is found in the electrolytes containing Cs^+, Li^+, Ba^{2+}, and Ca^{2+}. In fact, this shows that these less acidic, weakly hydrated species lead to a good performance for the CO_2RR, in part, due to their sluggish activity for the water reduction reaction. It seems that multivalent acidic cations enhance the activity for CO, already at low overpotentials, but do not lead to a good performance at high overpotentials due to their extreme promotion of water reduction.

Although Figure 4c provides a qualitative comparison of the relative activity at low and high overpotentials, it does not allow to directly assess which electrolyte leads to the absolute highest activity for CO_2RR to CO. For that, we have compared the CO_2RR activity using pure electrolytes of the most promising species (at high overpotential), namely, 0.2 M M_xClO_4 electrolytes, with M^{n+} = Li^+, Cs^+, Ca^{2+}, and Ba^{2+}. We see in Figure 5 that at high overpotentials Cs^+ is the cation that leads to the largest amount of CO produced, due to its weak hydration shell, allowing Cs^+ to accumulate at the reaction interface. Additionally, as Cs^+ is a nonacidic cation, its enhancement on water reduction is not so large, favoring CO_2RR. Interestingly, we find that the activity in Ba^{2+} electrolyte is higher than in Li^+, even though Li^+ has more
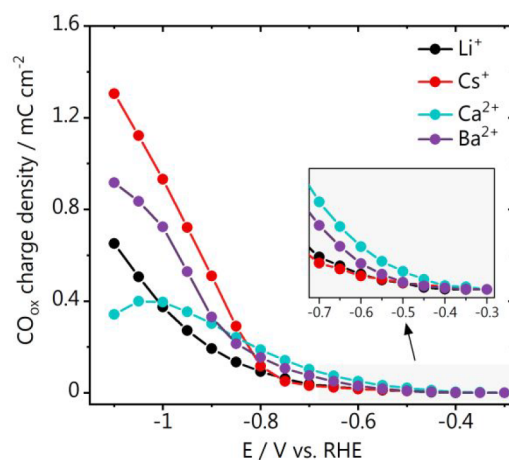

Figure 5. Amount of CO produced probed via consecutive cathodic/anodic cycling at pH 3 in 0.2 M_xClO_4 with M^{n+} = Li^+, Cs^+, Ca^{2+}, and Ba^{2+}.

positive hydration energy and is less acidic (see Figure S8). Here, the activity at low overpotentials (or equivalently in acidic electrolyte) is also found to be higher in the electrolytes containing the more acidic divalent species (Ca^{2+} and Ba^{2+}), in agreement with the results from Figure 4.

Computational Models. To model the competing processes occurring at the electrode/electrolyte interface, we employed AIMD simulations with the PBE+D2 functional.[35−37] We represented the experimental system as a $3\sqrt{3}{\times}3\sqrt{3}-R30°$ Au(111) supercell (4 layers, 15.3 Å × 15.3 Å × 30.0 Å) with 72 water molecules explicitly inserted within a 15 Å solvation layer and an additional 8 Å layer of vacuum. The solvation configuration was retrieved from our recent work,[25,52] where it was optimized for more than 10 ps (time step of 1 fs) at 300 K. Details on the density functional theory setup, as well as AIMD parameters, are available in the "density functional theory modeling" section in the Experimental Section and in the Supporting Information. We inserted two atoms from six different species (M = Li, Cs, Mg, Ba, Al, Nd) within the solvation layer, at an initial distance from the surface of 3.3 Å. Since each species donates n electrons to the simulation cell depending on its valence (M^{n+}), we removed $2n$ hydrogens from the fourth water bilayer to ensure charge balance (−$2n$ |e⁻| of $2n$ OH⁻ vs +$2n$ |e⁻| of 2 M^{n+}). Thus, these models described six different Au/water/M^{n+} systems (M^{n+} = Li^+, Cs^+, Mg^{2+}, Ba^{2+}, Al^{3+}, Nd^{3+}), with cation coverages of 0.07 ML (2/27), equivalent to 1.0−1.6 molar concentration. The six systems were further optimized for 2 ps at 300 K applying an electric field of −0.3 V Å⁻¹,[38,53] to mimic local electric field effects.[22,54] The applied electric field roughly corresponds to −0.9 V vs the potential of zero charge, thus −0.7 V vs SHE in case of polycrystalline gold (see the SI).

To validate our methodology and confirm the convergence of the Au/water/M^{n+} systems despite the short simulation time, we first analyzed the structural properties of multivalent cations during the first 2 ps of equilibration. The cation coordination shell showed excellent agreement with experimental data.[55,56] By fitting the cation−water radial distribution functions (RDF) for all the AIMD snapshots during the 2 ps equilibration, we estimate an average cation−oxygen distance following the trend Al^{3+} < Li^+ < Mg^{2+} < Ba^{2+} < Cs^+, as reported in the literature (Figure S10, Table S1).[55,56] Besides, our
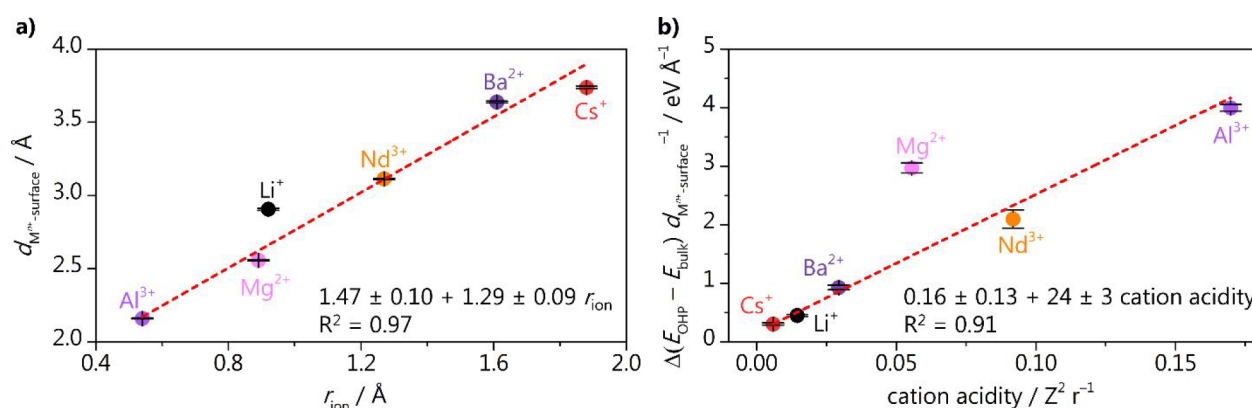
Figure 6. (a) Correlation between average cation−surface distance after 1 ps equilibration and cation ionic radius taken from literature values.[47] (b) Correlation between the calculated thermodynamic driving force for cation accumulation (with respect to cation−surface distance) and cation acidity. Uncertainties are given by the standard deviations of the data points (a) and the fit errors (b), respectively.
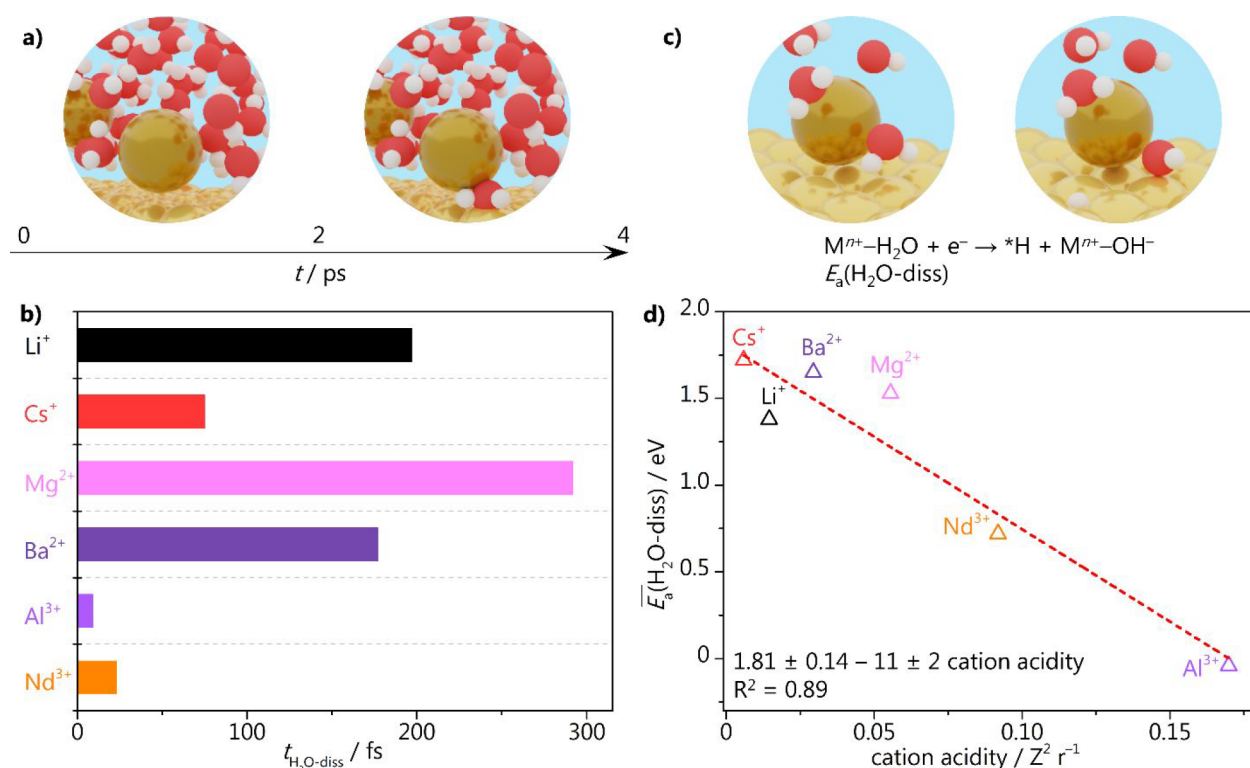

Figure 7. (a) Models for AIMD simulation performed at 300 K: equilibration of Au/water/M^{n+} systems (0−2 ps); equilibration of Au/water/M^{n+}/*H_2O (2−4 ps), with M^{n+} = Li^+, Cs^+, Mg^{2+}, Ba^{2+}, Al^{3+}, and Nd^{3+}. (b) Time required for dissociating adsorbed water upon interaction with M^{n+} during AIMD. (c) Models for initial and final states for water dissociation. (d) Activation barrier for water dissociation vs cation acidity, calculated as the average of the values for 2 and 3 H_2O molecules in the cation solvation shell. This process is barrierless for Al^{3+}. In panels (a) and (c), Au, Cs, H, and O atoms are portrayed as yellow, dark yellow, white, and red spheres, respectively.

model shows remarkable accuracy in reproducing the cation coordination environment. The coordination shell of Li^+ accounts for 3 or 4 water molecules, while Cs^+, Ba^{2+}, and Nd^{3+} exhibit higher water−cation coordination numbers respectively of 4−6, 6−8, and 4−6 (Figure S11 and Table S2). Finally, cation coordination numbers of 2 and 3 for Mg^{2+} and Al^{3+} are due to $Mg(OH)_2$ and $Al(OH)_3$ compounds that form on the surface, in excellent agreement with experimental observation of the tendency of small-radius acidic cations to form hydroxide layers upon alkalization of the interface (eq 3). Overall, cation coordination numbers converged to the experimental values after 0.5−0.6 ps of AIMD (Figure S11),

thus confirming that our model correctly reproduces the cation coordination environment.

Cation Accumulation at the OHP. Looking at the mobility of the different cations across the reaction interface, we see that all the species reach a stable position after 1 ps of initial equilibration (see Figure S12). Al^{3+} and Mg^{2+} cations get closer to the surface ($d_{Mn-surface}$ ≈ 2.1 Å and 2.5 Å, respectively), while Li^+, Nd^{3+}, Ba^{2+}, and Cs^+ exhibit larger distances (∼2.9, ∼3.1, ∼3.6, and ∼3.7 Å, respectively). Interestingly, this effect is seen only for one of the two cations in the cell, while the second one remains at 1−2 Å larger distance from the surface, likely due to steric hindrance or
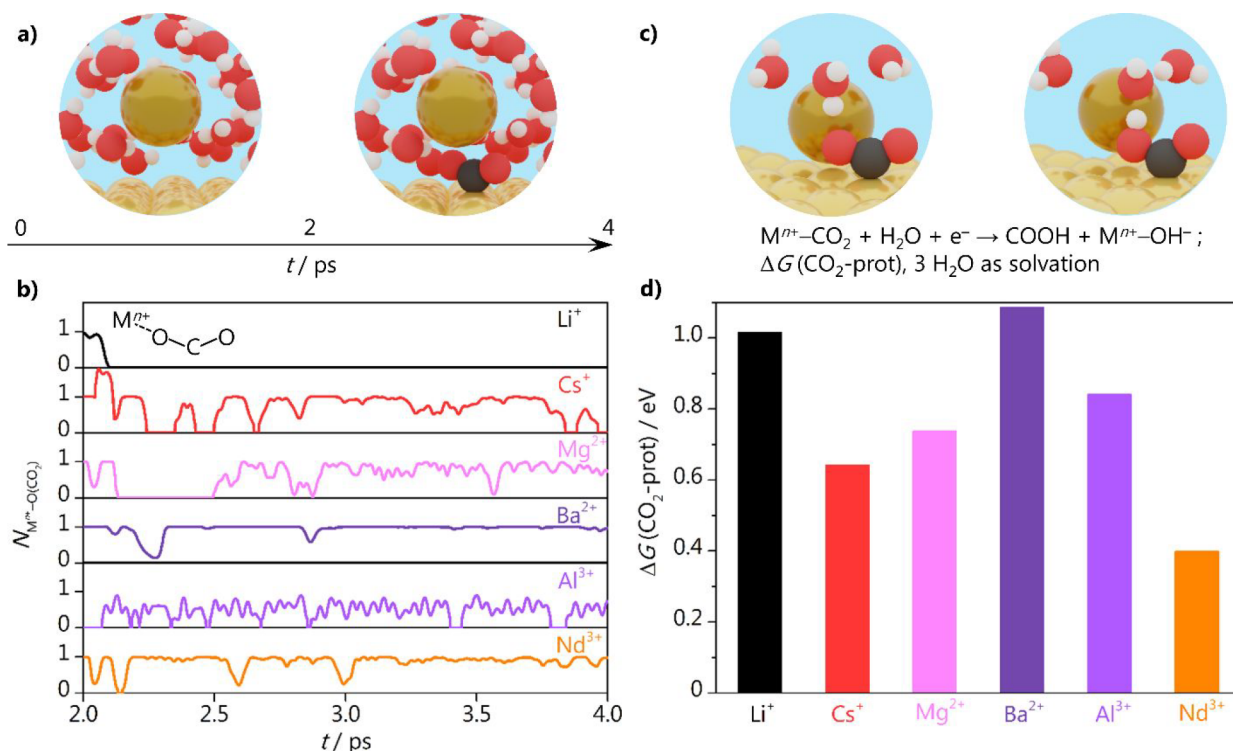
Figure 8. (a) Models for AIMD simulation performed at 300 K: equilibration of Au/water/M^{n+} systems (0−2 ps); equilibration of Au/water/M^{n+}/ *CO_2 (2−4 ps), with M^{n+} = Li^+, Cs^+, Mg^{2+}, Ba^{2+}, Al^{3+}, and Nd^{3+}. (b) Cation−CO_2 coordination ($N_{M^{n+}-O(CO2)}$) for 2 ps of AIMD simulation. (c) Model for initial and final state of CO_2 protonation. (d) Gibbs free energy required for COOH protonation. In panels (a) and (c), Au, Cs, C, H, and O atoms are portrayed as yellow, dark yellow, dark gray, white, and red spheres, respectively.

electrostatic repulsion. We find that the average cation−surface distances calculated after 1 ps equilibration correlate well with the cation ionic radius (Figure 6a), indicating that at the low cation concentrations assumed in this study (1.0−1.6 M), cations with a relatively small ionic radius locate closer to the surface due to their small solvation shell. Nevertheless, if we consider the thermodynamics associated with cation accumulation at the OHP, this process becomes increasingly hindered at higher cation concentrations (for acidic cations). To assess such an effect, we estimated the energy of a single cation at different cation−surface distances within the OHP, E_{OHP} ($d_{M-surface}$), by carrying out single-point DFT calculations on 50 AIMD snapshots (every 20 fs after 1 ps equilibration). The reference system was the gold supercell, the solvation layer, and the second cation. Then, we compared the estimated E_{OHP} to the energy of the cation at the bulk electrolyte, E_{bulk}, calculated according to the methodology introduced by Resasco et al.[24,25,57] (see the SI for further details). E_{OHP} − E_{bulk} thus gives an estimation of the thermodynamic driving force relative to cation accumulation at a given position within the OHP (Figure S13). Even though this process is exothermic for any cation species ($E_{OHP} − E_{bulk}$ < 0 eV), it becomes less favorable for shorter cation−surface distances, i.e., for cations closer to the surface. As qualitatively observed during the AIMD, cation−cation repulsion limits cation accumulation, and this phenomenon becomes extremely significant for acidic cations, which experience stronger repulsion. The driving force for cation accumulation decreases for Al^{3+}, Nd^{3+}, and Mg^{2+} when these species approach the surface, Figure S13; thus this parameter correlates negatively with the cation−surface distance (Table S3). Instead, nonacidic cations such as Li^+ and Cs^+ do not exhibit any strong dependence of $E_{OHP} − E_{bulk}$

vs cation position, due to their low valence and consequently minimal repulsion. Besides, the variation of driving force for cation accumulation with respect to $d_{M-surface}$ can be taken as a proxy of the cation−cation repulsion. Such gradient of accumulation driving force correlates with cation acidity (Figure 6b), suggesting that under realistic CO_2 reduction conditions nonacidic cations accumulate more at the OHP. Higher cation concentration due to accumulation at the OHP leads to more significant intrinsic promoting effects,[25] at least in acidic, neutral, or mildly alkaline pH. At high local alkalinity, as we recently reported,[14,58] high near-surface cation concentrations are detrimental to HER on gold and platinum, due to blockage of the surface, creating what we call the cation "inhibition regime". In the present work, we are still in the promotion regime, where we see that cation accumulation has different consequences for H_2O reduction and CO_2 reduction performance. Within the valence groups, higher H_2O reduction current densities are found for Cs^+, Ba^{2+}, and Nd^{3+} in contrast to Li^+, Mg^{2+}, and Al^{3+} (Figure 2a). For CO_2 reduction, we see higher activity for Nd^{3+} (low overpotential region) and Cs^+ (high overpotential region) in comparison to Al^{3+} and Li^+ (Figure 4c).

Mechanism of Cation Effect on H_2O and H_3O^+ Reduction. To study the effect of a neighboring cation on water reduction, we introduced an additional H_2O adsorbed on the surface close to one of the cations, with a surface coverage of 0.04 ML (1 molecule for 27 Au surface atoms); see Figure 7a. We let the resulting systems Au/water/M^{n+}/*H_2O (M^{n+} = Li^+, Cs^+, Mg^{2+}, Ba^{2+}, Al^{3+}, Nd^{3+}) equilibrate during 2 ps at 300 K with an explicit electric field of −0.3 V Å^{-1}.[38,53] Upon introduction of the additional adsorbed water molecule, we see that regardless of the specific coordination between metal

cations and adsorbed water, the dissociation of H_2O into OH^- and H^+ occurs (Figure S14). Besides this process, no significant change was observed for cation—surface distance and cation coordination shell (Figures S15—S17, Table S4). The kinetics of water dissociation can be estimated by the AIMD time required for this dissociation to take place, which followed the trend $Al^{3+} \sim Nd^{3+} < Cs^+ < Ba^{2+} < Li^+ < Mg^{2+}$ (Figure 7b). A similar trend was found experimentally for the water reduction activity, Figure 2a, and cation acidity was suggested as a potential descriptor for the performance. Thus, we assessed the potential role of cation acidity in promoting the Volmer step of water reduction, since this reaction is the rate-determining step. We estimated the kinetic barrier related to water dissociation on a simplified model accounting for the $3\sqrt{3}\times3\sqrt{3}-R30°$ Au(111) supercell (4 layers, 15.3 Å × 15.3 Å × 30.0 Å), one cation, one adsorbed water molecule, and a cation coordination shell of 2 and 3 water molecules, respectively (Figure 7c with 3 H_2O, further details on the model in the SI), and explicit electric field of -0.3 V Å^{-1}.[38,53] We chose such simplified coordination shells, since they were previously indicated as the optimal configurations for assessing adsorption energy.[59] $n-1$ hydrogens were removed from the solvation layer so that the supercell included only an extra electron, donated from the M^{n+} species. We find that the cation acidity is an accurate descriptor since the activation energy for water dissociation correlates well with it, as shown in Figure 7d. Since we considered two different models for the coordination shell, we plot in the figure the average between the activation barriers calculated respectively with 2 and 3 explicit H_2O. Water dissociation is close to barrierless in the presence of acidic cations, thus driving the outstanding H_2O reduction performance of, for example, Nd^{3+} and Al^{3+} (Figure 2a). As for the acidic surface pH regime (i.e., H_3O^+ as proton source),[60] the Gibbs free energy for H_3O^+ dissociation correlates with cation acidity as well (Figure S18), although exhibiting a weaker correlation. However, this process is exergonic for every cationic species ($\Delta G < -1.0$ eV) and is kinetically barrierless, thus supporting the absence of a cation effect on proton reduction (Figure 3a). Additionally, we find that the *H adsorption energy is also cation-independent, with $\Delta G_{*H} \approx +0.3$ eV for the different species studied.

Mechanism of Cation Effect on CO_2 Reduction. To extend the previous methodology to the case of CO_2 reduction, we introduced a CO_2 molecule to the initial Au/water/M^{n+} system, keeping the same surface coverage as for adsorbed water (0.04 ML, 1/27 ML) and optimizing the system for 2 ps at 300 K (Figure 8a) with an explicit electric field of -0.3 V Å^{-1}.[38,53] After this equilibration, CO_2 adsorbs on the surface via a η^1_C conformation (monodentate through the carbon) so that the oxygen atoms coordinate to the alkali cation and to water molecules through hydrogen bonds. The introduction of the adsorbate close to the cation does not affect its position, as suggested by the absence of a significant variation of the cation—surface distance for Au/water/M^{n+}/*CO_2 (Figure S19 in the SI). Along with alkali cations,[25] a cation···$O(CO_2)$ coordination is observed as well for di- and trivalent species. While Li^+ only coordinates with *CO_2^- for the first 0.1 ps, Cs^+, Mg^{2+}, Ba^{2+}, Al^{3+}, and Nd^{3+} steadily interact with it, accounting for average coordination numbers of 0.7 ± 0.4, 0.6 ± 0.4, 0.9 ± 0.2, 0.5 ± 0.2, and 0.9 ± 0.2 (Figure 8b, Table S5). Cs^+, Ba^{2+}, and Nd^{3+} present more steady coordination, and the extent of the coordination increases according to the cation valence: Cs^+ coordinates for around 1.1

ps, while the bi- and trivalent counterpart coordinate for 1.3 and 2 ps, respectively (Figure 8b). We did not detect any significant variation of the cation coordination shells upon insertion of CO_2 (Figure S20, Table S5), suggesting that the adsorbate does not promote any dehydration, as in fact only already-dehydrated cations can coordinate with the adsorbate. In our recent work we demonstrated that $M···O(CO_2)$ coordination triggers a short-range stabilization effect on *CO_2^- of around 0.5—0.6 eV,[25] which enables CO_2 electroreduction. Thus, the high CO_2 reduction activity for Nd^{3+} in the low-overpotential region and Ba^{2+} and Cs^+ in the high-overpotential region (Figure 4c) can be rationalized through this coordination-driven stabilizing effect. To investigate if cations have any promoting effect as well on the protonation of the CO_2^- intermediate, we estimated the kinetic barrier related to this process with an analogous computational setup to the water dissociation case ($3\sqrt{3}\times3\sqrt{3}-R30°$ Au(111), one cation, *CO_2, 3 explicit water molecules, explicit electric field of -0.3 V Å^{-1}); see Figure 8c. CO_2 protonation is barrierless for every cation species apart from Mg^{2+} and Al^{3+}. In the presence of Mg^{2+} and Al^{3+}, we observed kinetic barriers of around 0.7 and 1.5 eV, which may be due to the excessive stabilization of the *CO_2^- intermediate or repulsion between COOH and the acidic cations. This theoretical evidence may explain the low CO_2 reduction performance of Mg^{2+} and Al^{3+} compared to Ba^{2+} and Nd^{3+}, respectively, in addition to its lower accumulation. Overall, local repulsion between cation and protons leads to a thermodynamic energy cost for COOH protonation between 0.4 and 1.0 eV, with Cs^+ and Nd^{3+} accounting for the lowest values (Figure 8d), and it does not depend on the cation species. Since it is just slightly endothermic, this step can occur under CO_2 reduction potentials. To summarize, the differences in CO_2 reduction performance of different cation species at low and high overpotentials can be rationalized considering the competing water reduction, cation accumulation, and coordination-driven stabilization of *CO_2^-, while CO_2 protonation is cation independent. As a final remark on the intrinsic cation effect on H_2O and CO_2 reduction, we added a benchmark system where we replaced the two Li^+ atoms with two H^+, to assess the potential role of protons as reaction-driving cations. H^+ quickly recombines with solvent molecules to form a H_3O^+ species ($\Delta t < 0.3$ ps, Figure S21); however neither of these species exhibit any interaction with *H_2O and *CO_2 during 2 ps AIMD (Figures S14—S17, S19, and S20, Tables S4 and S5). This insight provides an additional validation of our previous work,[25] confirming that CO_2 electroreduction needs a metal cation to occur.

■ DISCUSSION

Previous work from Schizodimou and Kyriacou[26] and Ringe et al.[11] suggests that multivalent cations promote CO_2 reduction. However, these works did not discuss how the multivalent species affect the hydrogen evolution reaction, while we see that this competition actually determines the reaction selectivity. Our experimental results show that acidic (multivalent) cations only favor CO_2 reduction at low overpotentials (acidic media), while at high overpotentials (neutral/alkaline media) such trend overturns, and the activity for CO increases in the order $Ca^{2+} < Li^+ < Ba^{2+} < Cs^+$. As we proposed in our recent work,[25] an explicit coordination-driven short-range interaction stabilizes the *CO_2^- intermediate and enables CO_2 reduction independently from the cation species. In fact, the
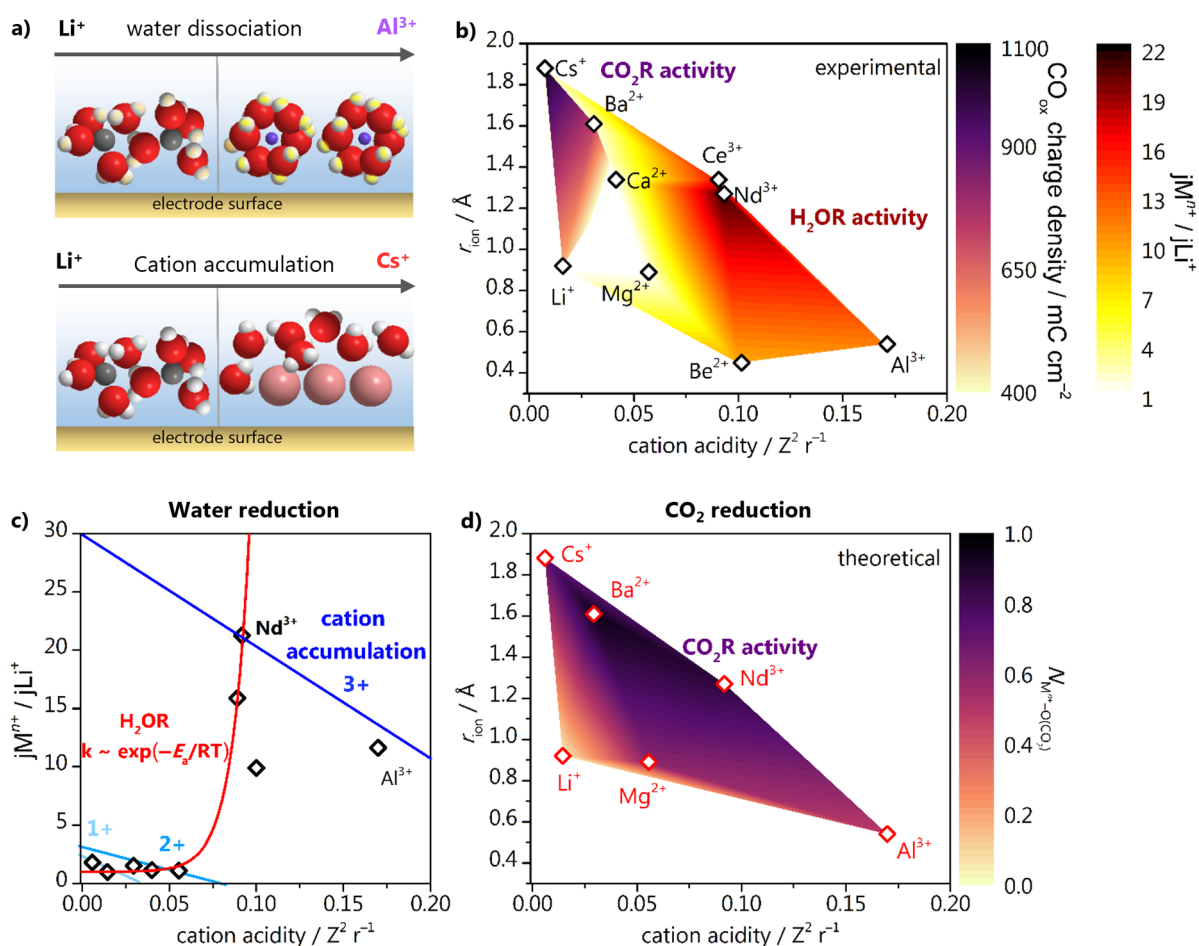
Figure 9. Schematic representation of (a) the interaction of different cation species with the electrode surface, leading to favorable water dissociation and higher accumulation at the OHP. (b) Colormap summarizing CO_2 reduction (purple shades, Figure 5) and H_2O reduction (red shades, Figure 2a) performances at high overpotential vs cation ionic radius and cation acidity. (c) Normalized activity for water reduction vs cation acidity and qualitative fit representing the interplay between water dissociation kinetics (red) and cation accumulation (shades of blue) for alkali (1+), divalent (2+), and trivalent (3+) species. (d) CO_2 reduction activity predicted assuming average cation–CO_2 coordination ($N_{M^{n+}-O(CO2)}$) (Table S5) as a potential descriptor vs ionic radius and cation acidity.

energy required for CO_2 activation ($\sim$0.2–0.4 eV)[25] is significantly lowered in the presence of alkali and di- and trivalent cations (Figure S22, Table S6). Thus, the CO_2 reduction activity solely correlates with the extent of such cation–CO_2 coordination. In general, trivalent cations exhibit more steady $M^{n+}\cdots O(CO_2)$ coordination than divalent and alkali cations, and this phenomenon is more significant for weakly hydrated cations (Figure 8b). This rationalizes the performances of Nd^{3+} and Al^{3+} vs Cs^+ and Ba^{2+} for CO_2RR at low- and high-overpotential regions, respectively. However, it does not explain the difference between the two potential regions. This difference must be attributed, instead, to the performance of these different cations for water reduction. From the results shown in Figure 2 we clearly see that trivalent species promote water reduction more than di- and monovalent cations. This can be elucidated by the stabilizing effect acidic cations have on the transition state of water dissociation, confirmed by the linear correlation between the water dissociation activation barrier and cation acidity (Figure 7d). Additionally, the reactivity of water molecules surrounding acidic cations comes from the same principle of how cations undergo hydrolysis. The positive charge of the metal cation draws the electron density of the oxygen of a water molecule toward the metal center, weakening the hydrogen

bond of the water molecule, thus lowering the barrier for water dissociation. In fact, water molecules adsorbed close to a cation species undergo hydrolysis in less than 200 fs during AIMD, and this effect is faster for more acidic cations (Figure 7b). We show schematically in the top panel of Figure 9a how, with a smaller cation ionic radius and a larger charge, the water molecules surrounding the cation will be more reactive. In the scheme, we show for instance that water dissociation is favored in the presence of Al^{3+} cations in comparison to Li^+, and the degree of such promotion is represented here by different intensities of yellow shades on the hydrogen atoms. Besides, the cation acidity dictates the cation hydration energy, which in turn governs how many cations will accumulate at the OHP. This is represented in the lower panel of Figure 9a, where we show that Cs^+ cations, since they are weakly hydrated, are present at the reaction interface in higher concentrations than more strongly hydrated and more acidic cations such as Li^+. This explains why in Figure 2 for the alkaline earth cations the highest activity for water reduction is found for Ba^{2+} (considering Be^{2+} an exception), and for the trivalent species for Nd^{3+} and Ce^{3+}. Analogously, for CO_2 reduction, Nd^{3+} outperforms Al^{3+} in the low-overpotential region, while the highest activities at high overpotential are observed for Cs^+ and Ba^{2+}. The loose water structure around these weakly hydrated

species prevents effective charge screening, thus allowing these cations to partially lose their hydration shell. By minimizing steric hindrance and electrostatic repulsion effects, Cs^+, Ba^{2+}, and Nd^{3+} accumulate more at the interface. Since the extent of cation repulsion correlates with cation acidity (Figure 6a), nonacidic cations are expected to be more concentrated at the OHP.

In Figure 9b we summarize the performance of alkali, di- and trivalent cations for H_2O and CO_2 reduction at high overpotential (Figure 2a, Figure 5). HER activity peaks for mildly acidic cations (red-shaded region in Figure 9b), such as Nd^{3+} and Ce^{3+}, and the rationale behind this trend lie in the activity volcano plot due to the interplay of water dissociation kinetics and cation accumulation (Figure 9c). The water dissociation activation barrier decreases for higher cation acidity (Figure 7d); consequently the rate of this step increases exponentially. However, strongly acidic cations such as Be^{2+} and Al^{3+} are limited by their low concentration at the OHP; thus the Nd^{3+} is the optimum, since it accumulates at the OHP and shows high enough reactions rates. As for CO_2 reduction, experimentally, Cs^+ and Ba^{2+} lead to the highest performance at high overpotentials (Figure 5, purple-shaded region in Figure 9b), while Nd^{3+} is in the sweet spot for the low-overpotential region. Theoretically, this trend can be reproduced assuming the average cation–CO_2 coordination number as the sole descriptor for CO_2 reduction activity in the absence of the competing water reduction reaction (Figure 9d). Again, nonacidic or mildly acidic cations exhibit a steady short-range interaction with the $*CO_2^-$ adsorbate, since they can effectively desolvate due to their low dehydration energy.

Finally, both our experimental and computational results demonstrate that water and proton reduction must be taken into account for an accurate prediction of the activity of CO_2RR, since a steady supply of water or protons is key to enable a quick protonation of the $*CO_2^-$ intermediate, but also can lead to a high activity for water reduction. When water reduction is not competing with CO_2RR (at low overpotentials or acidic media), acidic and weakly hydrated cations promote CO_2RR, while at high overpotentials (neutral/alkaline media) the commonly used Cs^+-containing electrolyte leads to the highest activity.

◼ CONCLUSIONS

In this work, we assessed the electrocatalytic CO_2 reduction and H_2O reduction activity in mildly acidic electrolytes (bulk pH = 3) containing Li^+, Cs^+, Be^{2+}, Mg^{2+}, Ca^{2+}, Ba^{2+}, Al^{3+}, Nd^{3+}, and Ce^{3+}. We observed that cations have no effect on proton reduction at low overpotentials. Instead, the activity and onset for the water reduction reaction correlate with cation acidity, so that weakly hydrated trivalent species lead to the highest activity. This observation is rationalized through an activity volcano plot, with one side of the volcano at low cation acidity limited by poor water dissociation kinetics, while the other side is hindered by low cation accumulation (Figure 9c). Consequently, acidic cations only favor CO_2 reduction at low overpotentials (acidic media), below potentials at which water reduction is active. At high overpotentials (neutral/alkaline media), the activity for CO production increases in the order $Ca^{2+} < Li^+ < Ba^{2+} < Cs^+$, showing an interplay between concentration at the outer Helmholtz plane, with specific cation-promoting effects on water dissociation and cation stabilization of $*CO_2^-$ determining the CO_2RR vs H_2O reduction competition. *Ab initio* molecular dynamics simu-

lations suggest that cation acidity determines cation accumulation at the OHP and water dissociation kinetics. Softly hydrated cations, such as Cs^+, Ba^{2+}, and Nd^{3+}, present minimal cation–cation repulsion so they accumulate at the OHP. Besides, in the presence of acidic cations, water dissociation is barrierless, thus explaining their outstanding water reduction performance. As for CO_2 reduction, a short-range interaction driven by coordination between cation and $*CO_2^-$ stabilizes this intermediate, thereby activating CO_2 for reduction. Trivalent cations and weakly hydrated species account for a more continuous coordination, thus a higher promoting effect. Hence, Cs^+, Ba^{2+}, and Nd^{3+} lead to higher CO_2RR activities than their strongly hydrated counterparts, following the trend $Cs^+ < Ba^{2+} < Nd^{3+}$. In summary, H_2O and CO_2 reduction performances are primarily ruled by cation accumulation at the OHP, which leads to higher concentrations and consequently higher rates of intrinsic cation-promoting effects. Cation accumulation correlates with cation acidity, so nonacidic cations are expected to have higher near-surface concentrations under CO_2 reduction conditions. As for intrinsic cation effects, trivalent cations promote both $*CO_2^-$ stabilization and water dissociation; thus they are active for CO_2 reduction only below potentials at which H_2O reduction is highly active. In contrast, Cs^+ and Ba^{2+} account for high CO_2 reduction activity at high overpotentials, since they can stabilize the $*CO_2^-$ intermediate, while they show poor kinetics for water dissociation.

Even though the application of multivalent cations in neutral/alkaline media is not practical, due to hydroxide deposition, they may in principle still be used for CO_2 electrolysis in strong acidic media. In fact, we have recently shown that CO_2RR to CO can be carried out at industrially relevant current densities in acidic media, using gas diffusion electrodes.[61] We obtained faradaic efficiencies for CO close to 90% at lower cell potentials than in neutral media. Future work could therefore focus on trying to improve the energy efficiency even further by adding small amounts of, for example, Nd^{3+} to a Cs^+ background electrolyte, in a way that hydroxide deposition would not be detrimental to the performance. Pulsed electrolysis also presents an opportunity for the use of multivalent cations for CO_2RR, as possible hydroxide deposits can dissolve in between cathodic pulses. Besides, theoretical works on CO_2 reduction should also consider the kinetics and thermodynamics of the water dissociation step to accurately model the hydrogen evolution reaction when water is the proton source, instead of using H binding as the sole descriptor.

The DFT data sets generated during the current study are available in the ioChem-BD database[62] at DOI: 10.19061/iochem-bd-1-213.

◼ ASSOCIATED CONTENT

ⓢ Supporting Information

The Supporting Information is available free of charge at https://pubs.acs.org/doi/10.1021/jacs.1c10171.

> Blank voltammograms of the gold electrode, additional cyclic voltammetry data, acidity vs hydration energy relationship, details on the DFT modeling, additional AIMD data (PDF)

■ AUTHOR INFORMATION

Corresponding Author

    Marc T. M. Koper − *Leiden Institute of Chemistry, Leiden University, 2300 RA, Leiden, The Netherlands;* ⊙ orcid.org/ 0000-0001-6777-4594; Email: m.koper@lic.leidenuniv.nl

Authors

    Mariana C. O. Monteiro − *Leiden Institute of Chemistry, Leiden University, 2300 RA, Leiden, The Netherlands;* ⊙ orcid.org/0000-0001-7451-1004

    Federico Dattila − *Institute of Chemical Research of Catalonia (ICIQ), The Barcelona Institute of Science and Technology (BIST), 43007 Tarragona, Spain;* ⊙ orcid.org/ 0000-0001-8195-3951

    Núria López − *Institute of Chemical Research of Catalonia (ICIQ), The Barcelona Institute of Science and Technology (BIST), 43007 Tarragona, Spain;* ⊙ orcid.org/0000-0001-9150-5941

Complete contact information is available at:
https://pubs.acs.org/10.1021/jacs.1c10171

Author Contributions

All authors read and commented on the manuscript. M.C.O.M. and F.D. contributed equally. All authors have given approval to the final version of the manuscript.

Notes

The authors declare no competing financial interest.

■ ACKNOWLEDGMENTS

■ REFERENCES

(1) Birdja, Y. Y.; Pérez-Gallent, E.; Figueiredo, M. C.; Göttle, A. J.; Calle-Vallejo, F.; Koper, M. T. M. Advances and Challenges in Understanding the Electrocatalytic Conversion of Carbon Dioxide to Fuels. *Nat. Energy* **2019**, *4* (9), 732−745.

(2) Resasco, J.; Bell, A. T. Electrocatalytic CO_2 Reduction to Fuels: Progress and Opportunities. *Trends Chem.* **2020**, *2* (9), 825−836.

(3) Smith, W. A.; Burdyny, T.; Vermaas, D. A.; Geerlings, H. Pathways to Industrial-Scale Fuel Out of Thin Air from CO_2 Electrolysis. *Joule* **2019**, *3* (8), 1822−1834.

(4) Zhang, Y. J.; Sethuraman, V.; Michalsky, R.; Peterson, A. A. Competition between CO_2 Reduction and H_2 Evolution on Transition-Metal Electrocatalysts. *ACS Catal.* **2014**, *4* (10), 3742−3748.

(5) Ooka, H.; Figueiredo, M. C.; Koper, M. T. M. Competition between Hydrogen Evolution and Carbon Dioxide Reduction on Copper Electrodes in Mildly Acidic Media. *Langmuir* **2017**, *33* (37), 9307−9313.

(6) Goyal, A.; Marcandalli, G.; Mints, V. A.; Koper, M. T. M. Competition between CO_2 Reduction and Hydrogen Evolution on a Gold Electrode under Well-Defined Mass Transport Conditions. *J. Am. Chem. Soc.* **2020**, *142* (9), 4154−4161.

(7) Hall, A. S.; Yoon, Y.; Wuttig, A.; Surendranath, Y. Mesostructure-Induced Selectivity in CO_2 Reduction Catalysis. *J. Am. Chem. Soc.* **2015**, *137* (47), 14834−14837.

(8) Welch, A. J.; Duchene, J. S.; Tagliabue, G.; Davoyan, A.; Cheng, W. H.; Atwater, H. A. Nanoporous Gold as a Highly Selective and Active Carbon Dioxide Reduction Catalyst. *ACS Appl. Energy Mater.* **2019**, *2* (1), 164−170.

(9) Kim, C.; Möller, T.; Schmidt, J.; Thomas, A.; Strasser, P. Suppression of Competing Reaction Channels by Pb Adatom Decoration of Catalytically Active Cu Surfaces during CO_2 Electro-reduction. *ACS Catal.* **2019**, *9* (2), 1482−1488.

(10) Moura de Salles Pupo, M.; Kortlever, R. Electrolyte Effects on the Electrochemical Reduction of CO_2. *ChemPhysChem* **2019**, *20* (22), 2926−2935.

(11) Ringe, S.; Clark, E. L.; Resasco, J.; Walton, A.; Seger, B.; Bell, A. T.; Chan, K. Understanding Cation Effects in Electrochemical CO_2 Reduction. *Energy Environ. Sci.* **2019**, *12* (10), 3001−3014.

(12) König, M.; Vaes, J.; Klemm, E.; Pant, D. Solvents and Supporting Electrolytes in the Electrocatalytic Reduction of CO_2. *iScience* **2019**, *19*, 135−160.

(13) Wang, Y.; Liu, X.; Liu, J.; Al-Mamun, M.; Wee-Chung Liew, A.; Yin, H.; Wen, W.; Zhong, Y. L.; Liu, P.; Zhao, H. Electrolyte Effect on Electrocatalytic Hydrogen Evolution Performance of One-Dimensional Cobalt-Dithiolene Metal-Organic Frameworks: A Theoretical Perspective. *ACS Appl. Energy Mater.* **2018**, *1* (4), 1688−1694.

(14) Goyal, A.; Koper, M. T. M. The Interrelated Effect of Cations and Electrolyte pH on the Hydrogen Evolution Reaction on Gold Electrodes in Alkaline Media. *Angew. Chem., Int. Ed.* **2021**, *60* (24), 13452−13462.

(15) Murata, A.; Hori, Y. Product Selectivity Affected by Cationic Species in Electrochemical Reduction of CO_2 and CO at a Cu Electrode. *Bull. Chem. Soc. Jpn.* **1991**, *64* (1), 123−127.

(16) Hori, Y.; Suzuki, S. Electrolytic Reduction of Carbon Dioxide at Mercury Electrode in Aqueous Solution. *Bull. Chem. Soc. Jpn.* **1982**, *55* (3), 660−665.

(17) Hori, Y.; Murata, A.; Takahashi, R. Formation of Hydrocarbons in the Electrochemical Reduction of Carbon Dioxide at a Copper Electrode in Aqueous Solution. *J. Chem. Soc., Faraday Trans. 1* **1989**, *85* (8), 2309.

(18) Thorson, M. R.; Siil, K. I.; Kenis, P. J. A. Effect of Cations on the Electrochemical Conversion of CO2 to CO. *J. Electrochem. Soc.* **2013**, *160* (1), F69−F74.

(19) Kim, H.; Park, H. S.; Hwang, Y. J.; Min, B. K. Surface-Morphology-Dependent Electrolyte Effects on Gold-Catalyzed Electrochemical CO_2 Reduction. *J. Phys. Chem. C* **2017**, *121* (41), 22637−22643.

(20) Zhang, B. A.; Costentin, C.; Nocera, D. G. Driving Force Dependence of Inner-Sphere Electron Transfer for the Reduction of CO_2 on a Gold Electrode. *J. Chem. Phys.* **2020**, *153* (9), 094701.

(21) Ayemoba, O.; Cuesta, A. Spectroscopic Evidence of Size-Dependent Buffering of Interfacial pH by Cation Hydrolysis during CO_2 Electroreduction. *ACS Appl. Mater. Interfaces* **2017**, *9* (33), 27377−27382.

(22) Chen, L. D.; Urushihara, M.; Chan, K.; Nørskov, J. K. Electric Field Effects in Electrochemical CO_2 Reduction. *ACS Catal.* **2016**, *6* (10), 7133−7139.

(23) Hussain, G.; Pérez-Martínez, L.; Le, J.-B.; Papasizza, M.; Cabello, G.; Cheng, J.; Cuesta, A. How Cations Determine the Interfacial Potential Profile: Relevance for the CO_2 Reduction Reaction. *Electrochim. Acta* **2019**, *327*, 135055.

(24) Resasco, J.; Chen, L. D.; Clark, E.; Tsai, C.; Hahn, C.; Jaramillo, T. F.; Chan, K.; Bell, A. T. Promoter Effects of Alkali Metal Cations on the Electrochemical Reduction of Carbon Dioxide. *J. Am. Chem. Soc.* **2017**, *139* (32), 11277−11287.

(25) Monteiro, M. C. O.; Dattila, F.; Hagedoorn, B.; García-Muelas, R.; López, N.; Koper, M. T. M. Absence of CO_2 Electroreduction on Copper, Gold and Silver Electrodes without Metal Cations in Solution. *Nat. Catal.* **2021**, *4* (8), 654−662.

(26) Schizodimou, A.; Kyriacou, G. Acceleration of the Reduction of Carbon Dioxide in the Presence of Multivalent Cations. *Electrochim. Acta* **2012**, *78*, 171−176.

(27) Banerjee, S.; Zhang, Z.; Hall, A. S.; Thoi, V. S. Surfactant Perturbation of Cation Interactions at the Electrode−Electrolyte Interface in Carbon Dioxide Reduction. *ACS Catal.* **2020**, *10* (17), 9907−9914.

(28) Monteiro, M. C. O.; Koper, M. T. M. Alumina Contamination through Polishing and Its Effect on Hydrogen Evolution on Gold Electrodes. *Electrochim. Acta* **2019**, *325*, 134915.

(29) Bhargava, S. S.; Cofell, E. R.; Chumble, P.; Azmoodeh, D.; Someshwar, S.; Kenis, P. J. A. Exploring Multivalent Cations-Based Electrolytes for CO₂ Electroreduction. *Electrochim. Acta* **2021**, *394*, 139055.

(30) Xue, S.; Garlyyev, B.; Watzele, S.; Liang, Y.; Fichtner, J.; Pohl, M. D.; Bandarenka, A. S. Influence of Alkali Metal Cations on the Hydrogen Evolution Reaction Activity of Pt, Ir, Au, and Ag Electrodes in Alkaline Electrolytes. *ChemElectroChem* **2018**, *5* (17), 2326−2329.

(31) Li, X.; Gunathunge, C. M.; Agrawal, N.; Montalvo-Castro, H.; Jin, J.; Janik, M. J.; Waegele, M. M. Impact of Alkali Metal Cations and Iron Impurities on the Evolution of Hydrogen on Cu Electrodes in Alkaline Electrolytes. *J. Electrochem. Soc.* **2020**, *167* (10), 106505.

(32) Do, U. P.; Seland, F.; Johannessen, E. A. The Real Area of Nanoporous Catalytic Surfaces of Gold and Palladium in Aqueous Solutions. *J. Electrochem. Soc.* **2018**, *165* (5), H219−H228.

(33) Kresse, G.; Furthmüller, J. Efficient Iterative Schemes for Ab Initio Total-Energy Calculations Using a Plane-Wave Basis Set. *Phys. Rev. B: Condens. Matter Mater. Phys.* **1996**, *54*, 11169−11186.

(34) Kresse, G.; Furthmüller, J. Efficiency of Ab-Initio Total Energy Calculations for Metals and Semiconductors Using a Plane-Wave Basis Set. *Comput. Mater. Sci.* **1996**, *6*, 15−50.

(35) Perdew, J. P.; Burke, K.; Ernzerhof, M. Generalized Gradient Approximation Made Simple. *Phys. Rev. Lett.* **1996**, *77*, 3865−3868.

(36) Grimme, S. Semiempirical GGA-Type Density Functional Constructed with a Long-Range Dispersion Correction. *J. Comput. Chem.* **2006**, *27*, 1787−1799.

(37) Bucko, T.; Hafner, J.; Lebègue, S.; Ángyán, J. G. Improved Description of the Structure of Molecular and Layered Crystals: Ab Initio DFT Calculations with van Der Waals Corrections. *J. Phys. Chem. A* **2010**, *114*, 11814−11824.

(38) Almora-Barrios, N.; Carchini, G.; Błoński, P.; López, N. Costless Derivation of Dispersion Coefficients for Metal Surfaces. *J. Chem. Theory Comput.* **2014**, *10*, 5002−5009.

(39) Blöchl, P. E. Projector Augmented-Wave Method. *Phys. Rev. B: Condens. Matter Mater. Phys.* **1994**, *50*, 17953−17979.

(40) Kresse, G.; Joubert, D. From Ultrasoft Pseudopotentials to the Projector Augmented-Wave Method. *Phys. Rev. B: Condens. Matter Mater. Phys.* **1999**, *59*, 1758−1775.

(41) Marx, D.; Hutter, J. *Ab Initio Molecular Dynamics: Basic Theory and Advanced Methods*; Cambridge University Press, 2009.

(42) Nosé, S. A Unified Formulation of the Constant Temperature Molecular Dynamics Methods. *J. Chem. Phys.* **1984**, *81*, 511−519.

(43) Hoover, W. G. Canonical Dynamics: Equilibrium Phase-Space Distributions. *Phys. Rev. A: At., Mol, Opt. Phys.* **1985**, *31*, 1695−1697.

(44) Dudarev, S. L.; Botton, G. A.; Savrasov, S. Y.; Humphreys, C. J.; Sutton, A. P. Electron-Energy-Loss Spectra and the Structural Stability of Nickel Oxide: An LSDA+U Study. *Phys. Rev. B: Condens. Matter Mater. Phys.* **1998**, *57* (3), 1505−1509.

(45) Kozub, A. L.; Shick, A. B.; Máca, F.; Kolorenč, J.; Lichtenstein, A. I. Electronic Structure and Magnetism of Samarium and Neodymium Adatoms on Free-Standing Graphene. *Phys. Rev. B: Condens. Matter Mater. Phys.* **2016**, *94* (12), 125113.

(46) Born, M. Volumen Und Hydratationswärme Der Ionen. *Eur. Phys. J. A* **1920**, *1* (1), 45−48.

(47) Lide, D. R. *CRC Handbook of Chemistry and Physics*, 84th ed.; CRC Press, 2003; Vol. 85.

(48) Alderighi, L.; Gans, P.; Midollini, S.; Vacca, A. Aqueous Solution Chemistry of Beryllium. *Adv. Inorg. Chem.* **2000**, *50*, 109−172.

(49) Rudolph, W. W. Raman and Infrared Spectroscopic Investigation of Speciation in BeSO₄(aq). *J. Solution Chem.* **2010**, *39* (7), 1039−1059.

(50) Hao, L.; Lu, R.; Leaist, D. G. Diffusion with Hydrolysis and Ion Association in Aqueous Solutions of Beryllium Sulfate. *J. Solution Chem.* **1996**, *25* (3), 231−242.

(51) Ekberg, C.; Brown, P. L. *Hydrolysis of Metal Ions*, Vol 1; Wiley-VCH Verlag GmbH & Co. KGaA: Germany, 2016.

(52) Dattila, F. Cation-Effect-CO₂-Reduction. *ioChem-BD* **2021**, 229432 DOI: 10.19061/iochem-bd-1-194.

(53) Feibelman, P. J. Surface-Diffusion Mechanism versus Electric Field: Pt/Pt(001). *Phys. Rev. B: Condens. Matter Mater. Phys.* **2001**, *64* (12), 125403.

(54) McCrum, I. T.; Bondue, C. J.; Koper, M. T. M. Hydrogen-Induced Step-Edge Roughening of Platinum Electrode Surfaces. *J. Phys. Chem. Lett.* **2019**, *10* (21), 6842−6849.

(55) Waegele, M. M.; Gunathunge, C. M.; Li, J.; Li, X. How Cations Affect the Electric Double Layer and the Rates and Selectivity of Electrocatalytic Processes. *J. Chem. Phys.* **2019**, *151* (16), 160902.

(56) Marcus, Y. Ionic Radii in Aqueous Solutions. *Chem. Rev.* **1988**, *88* (8), 1475−1498.

(57) Nørskov, J. K.; Rossmeisl, J.; Logadottir, A.; Lindqvist, L.; Kitchin, J. R.; Bligaard, T.; Jónsson, H. Origin of the Overpotential for Oxygen Reduction at a Fuel-Cell Cathode. *J. Phys. Chem. B* **2004**, *108* (46), 17886−17892.

(58) Monteiro, M. C. O.; Goyal, A.; Moerland, P.; Koper, M. T. M. Understanding Cation Trends for Hydrogen Evolution on Platinum and Gold Electrodes in Alkaline Media. *ACS Catal.* **2021**, *11* (23), 14328−14335.

(59) Garcia-Ratés, M.; García-Muelas, R.; López, N. Solvation Effects on Methanol Decomposition on Pd(111), Pt(111), and Ru(0001). *J. Phys. Chem. C* **2017**, *121* (25), 13803−13809.

(60) Dubouis, N.; Grimaud, A. The Hydrogen Evolution Reaction: From Material to Interfacial Descriptors. *Chem. Sci.* **2019**, *10* (40), 9165−9181.

(61) Monteiro, M. C. O.; Philips, M. F.; Schouten, K. J. P.; Koper, M. T. M. Efficiency and Selectivity of CO₂ Reduction to CO on Gold Gas Diffusion Electrodes in Acidic Media. *Nat. Commun.* **2021**, *12* (1), 4943.

(62) Álvarez-Moreno, M.; de Graaf, C.; López, N.; Maseras, F.; Poblet, J. M.; Bo, C. Managing the Computational Chemistry Big Data Problem: The IoChem-BD Platform. *J. Chem. Inf. Model.* **2015**, *55* (1), 95−103.